3D Characterization for Your 3D Material Structures.

- See even smaller sub-micron details
- Unprecedented image clarity at unprecedented speed enabled by AI
- UX designed for novices and experts alike

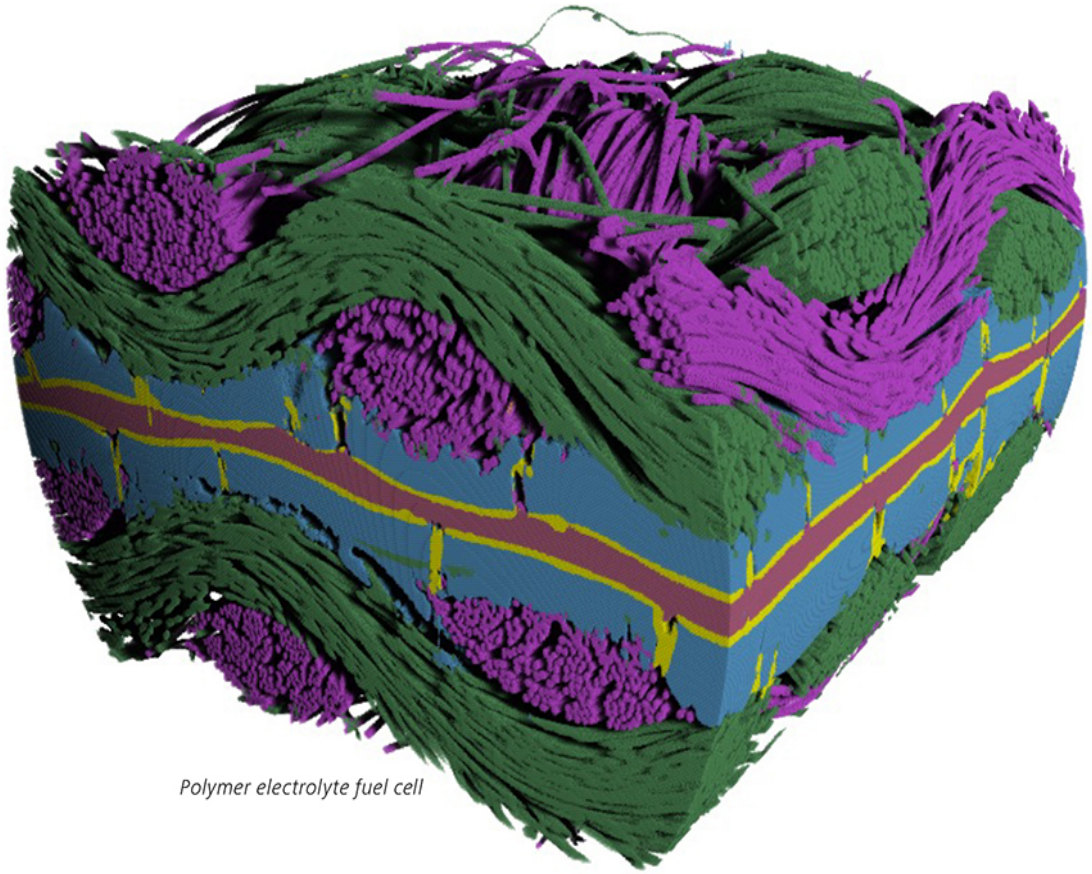

Polymer electrolyte fuel cell

Introducing ZEISS Xradia 630 Versa 3D X-ray Microscope

Seeing inside advanced materials can provide critical clues related to how structure affects performance. Achieving this insight at the microscale requires the clearest and highest-resolution 3D X-ray images. Use the newest ZEISS Xradia Versa 3D X-ray microscope (XRM) for nondestructive characterization of the finest sub-micron features within your materials. Leverage deep learning for the clearest 3D images across large representative volumes. Enjoy an intuitive, guided user experience that makes XRM technology accessible to all user skill levels.

ZEISS

Seeing beyond

Title: Electrochemical Healing of Fractured Metals

Authors: Zakaria Hsain[1], Mostafa Akbari[2], Adhokshid Prasanna[1], Zhimin Jiang[1], Masoud Akbarzadeh[2], James H. Pikul[1*]

Affiliations:
[1] Department of Mechanical Engineering and Applied Mechanics, School of Engineering and Applied Science, University of Pennsylvania, Philadelphia, PA, USA
[2] Department of Architecture, Weitzman School of Design, University of Pennsylvania, Philadelphia, PA, USA
(*) Author to whom correspondence should be addressed: pikul@seas.upenn.edu

Keywords: electrodeposition, healing, repair, structural metals, 3D printing, circular economy.

Abstract

Repairing fractured metals to extend their useful lifetimes advances sustainability and mitigates greenhouse gas emissions from metal mining and processing. While high-temperature techniques have long been used to repair metals, the increasing ubiquity of digital manufacturing and "unweldable" alloys, as well as the integration of metals with polymers and electronics, call for radically different repair approaches. This paper presents a framework for effective room temperature repair of fractured metals using an area-selective nickel electrodeposition process we refer to as electrochemical healing. Based on a theoretical model that links geometric, mechanical, and electrochemical parameters to the recovery of tensile strength, this framework enables 100% recovery of tensile strength in nickel, low-carbon steel, two "unweldable" aluminum alloys, and a 3D-printed difficult-to-weld shellular structure while using a single common electrolyte chemistry. Through a distinct energy dissipation mechanism, this framework also enables up to 136 % recovery of toughness in an aluminum alloy. To facilitate practical adoption, this work reveals scaling laws for the energetic, financial, and time costs of healing, and demonstrates the restoration of a functional level of strength in a fractured standard steel wrench. Empowered with this framework, room-temperature electrochemical healing could open exciting possibilities for the effective, scalable repair of metals in diverse applications.

Introduction

Annually, the mining, refining, and processing of structural metals result in over 3 billion tons of CO_2-equivalent emissions, and the mining and refining of aluminum, alone,

This article has been accepted for publication and undergone full peer review but has not been through the copyediting, typesetting, pagination and proofreading process, which may lead to differences between this version and the Version of Record. Please cite this article as doi: 10.1002/adma.202211242.

produces over 14,000 tons of largely toxic byproducts [1–4]. Improving the sustainability of structural metals, through a circular economic model based on recycling, refurbishing, repair, and reuse [5], could play an important role in mitigating greenhouse gas emissions and addressing many detrimental ecological effects [1,4,6] **(Fig. 1a)**. Repair, in particular, not only extends the operational lifetime of metal structures, thus reducing waste from end-of-life disposal and byproducts of mining and refining [4,7,8] **(Fig. 1a)**, but also complements recycling, which is limited by the difficulty of removing elemental contaminants from alloys and multi-metal parts [9].

For the past 6,000 years, high-temperature techniques, such as brazing and welding [10–12], have enabled metal repair without the high resource costs of melting and recasting fractured parts. Recent innovations in repairable and self-healing metals have exploited joule heating[13,14], phase transitions[15–17], solute precipitation[18,19], combined phase transitions and precipitation[20], and exothermic reactions[21]. These innovative techniques, along with the established techniques of welding and brazing, remain limited by the need for high temperature to make metal atoms mobile and the resulting high energy input, as well as by either the low strength of healed metals, the small size of repairable cracks, or the constrained microstructure and chemical composition of healed metals.

Notably, welding suffers from distinct limitations that are accentuated by recent advances in digital manufacturing and material integration, which calls for radically different approaches to repair metals. Several metallic alloys, including aluminum alloys of the 2000, 6000, and 7000 series [22,23] and nickel superalloys with Al and Ti concentrations in excess of 4 wt.% [24], are considered "unweldable" as they are vulnerable to cracking due to extreme thermal gradients and solute segregation [25,26] **(Fig. 1b)**. Approaches have been developed to mitigate these limitations [22,25,27,28], however, high levels of operator skill, experience, and precision are required, which may limit the wide adoption of welding in a decentralized circular economy. Posing further challenges to welding are recent advances in design [29,30] and additive manufacturing [31–34] which have enabled metal structures with high levels of geometric complexity. The octet-truss lattice shown in **Fig. 1c** is an example of a complex geometry where a fracture in an internal strut cannot be readily accessed by a welding torch (or beam). Moreover, the high temperatures induced by welding can cause damage to nearby non-metallic materials, as metals are increasingly integrated with polymers [35,36] or electronics [37–39] in various aerospace, robotic, and sensing applications.

By enabling fast room-temperature diffusion of metal ions in an aqueous medium (10^{-9} m^2 s^{-1}), electrochemical healing represents a fundamentally different approach to repair fractured structural metals [40–42]. Coating a metal structure with a passivating coating ensures that metal ions are only reduced at fracture sites, thus resulting in efficient targeted healing **(Bottom insets of Fig. 1c)**. Using this approach, electrochemical plating of nickel has shown promise, by enabling 100 % recovery of tensile strength in fractured cellular nickel (or nickel foam), with minimal energy use (~10^2 J per mm of crack length) compared to many high-temperature healing techniques (up to 10^9 J/mm) [40]. However, prior attempts to repair bulk metals using nickel plating failed to recover 100 % of pristine tensile strength due to poor nickel-metal adhesion or defects caused by diffusion-limited plating [41–44]. To become a

credible alternative to welding, electrochemical healing should ideally employ a simple process with a single electrolyte chemistry to effectively repair a wide variety of structural metals beyond nickel (including complex 3D printed structures and "unweldable" alloys) within a quantitative predictive framework. Prior work on the electrochemical joining of metal parts achieved high adhesion of plated nickel to other metals, but required multi-step processes with acid pre-treatments and plating in different electrolyte chemistries, and did not present a model that predicted or provided understanding of how to achieve optimal mechanical properties of the joined parts [45–49].

Here, we propose a framework for electrochemical healing, based on an experimentally validated theoretical model that elucidates the geometric, electrochemical, and mechanical parameters needed for 100% recovery of tensile strength in fully fractured structural metals. This framework enables the full restoration of tensile strength in nickel, low-carbon steel, two "unweldable" aluminum alloys, and a difficult-to-weld 3D printed funicular shellular structure. This framework shows the possibility of over 100% recovery of toughness (or work of fracture) in fractured metals subject to tensile loading. To facilitate practical adoption, we demonstrate the effective repair of a fully fractured steel wrench, and propose scaling laws for the energetic, financial, and time costs of repairing metals from the microscale to the meter-scale.

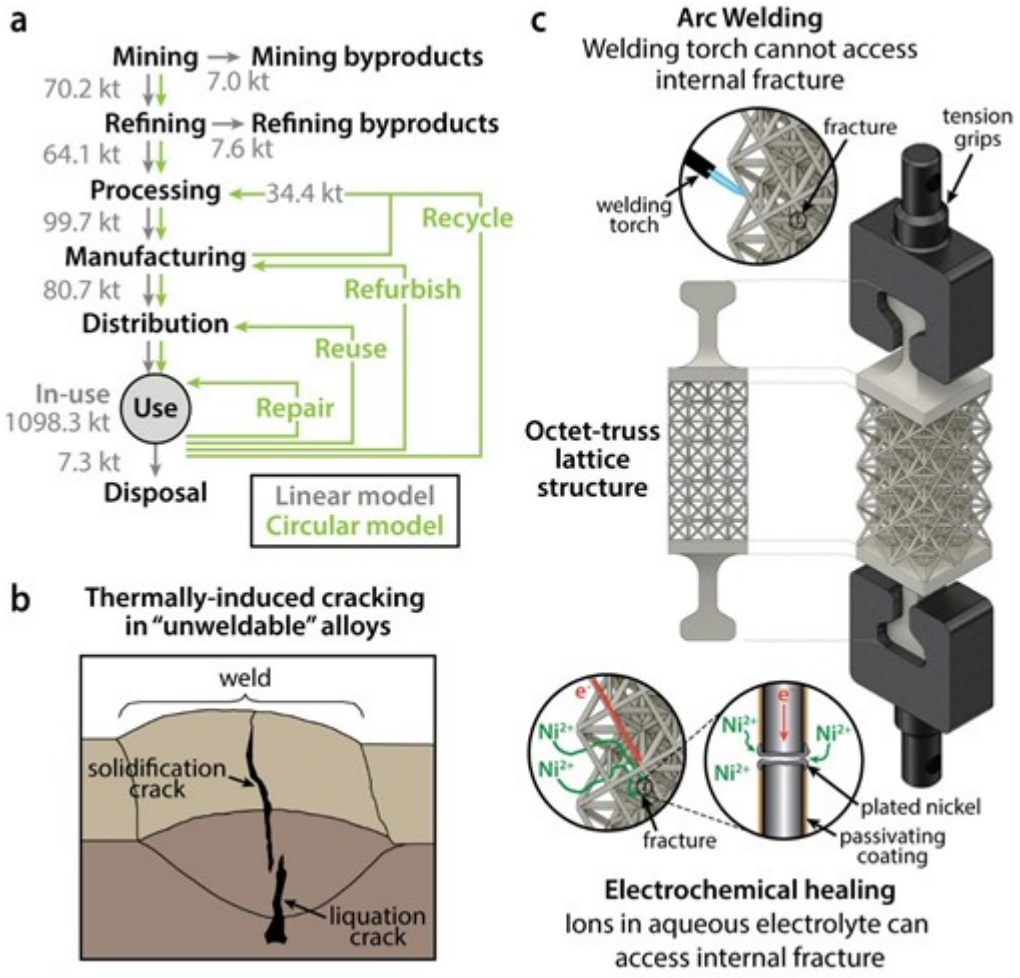

Fig 1. Limitations of welding as a repair technique in a metals circular economy. (a) Life cycle of structural metal parts under a linear model and a sustainable circular model with 2019 numbers for aluminum (in kilotons) from the International Aluminum Institute (ref. 8). (b) Illustration of thermal cracking resulting from welding "unweldable" alloys. (c) 3D rendering of an octet-truss lattice structure. Top inset shows that a conventional welding torch cannot access a fracture in an internal strut. Bottom insets show how nickel ions can easily access the fractured internal strut, where they are reduced to nickel metal during electrochemical healing. A passivating coating enables targeted electrochemical reduction at the fracture site.

Results and Discussion

Fig. 2a illustrates our approach to electrochemically heal structural metals. We describe this process as electrochemical healing because of its similarity to bone healing, where healing matter is transported to the fracture site through an immersed electrolyte and strength is restored through the growth and connection of matter from opposite fracture surfaces [40]. As an improvement over earlier approaches in which metal was only plated at the cross-section of a fractured strut [40,41], we exposed the non-fractured surface of the metal to plating **(Fig. 2a)**. A pair of Ni 200 (> 99% nickel alloy) half-dogbone samples prepared by waterjet cutting simulated a fractured dogbone sample **(Figs. 2a, S2 A)**. Insulating electric tape masked the fractured sample so that only a fraction, $A_e/2$, of the total available area,

A_o/2, in each half-dogbone was exposed **(Figs. 2a, S2 B)**. A custom fixture **(Fig. S2 D)** held the fractured sample in a nickel sulfamate aqueous electrolyte in alignment and with no gap at the fracture. Our prior work showed that minimizing the fracture gap is essential to achieving effective healing with minimal time and charge input [41]. Applying a constant potential of -1.8 V vs. Ni to the fractured sample resulted in nickel deposition over the entire exposed area A_e, with the amount of plating controlled by the charge input Q **(Figs. 2a, S2 C)**.

After removing the masking tape, healed Ni 200 samples were tested in tension until fracture. **Fig. 2b** shows the resulting stress-strain data for two samples healed with 200 mAh and 1000 mAh, alongside the stress-strain data of a pristine sample for reference. To assess the effectiveness of the healing process, we compared the tensile strength of each healed sample, σ_U, with the average tensile strength of five pristine samples, σ_M **(Table S3)**. Samples healed with Q = 1000 mAh exhibited an increase in strength healing efficiency σ_U/σ_M as A_e increased, eventually reaching a plateau at σ_U/σ_M = 1, or full restoration of pristine tensile strength **(Fig. 2c)**. In contrast, samples healed with Q = 200 mAh exhibited an increase in σ_U/σ_M reaching a maximum of σ_U/σ_M = 0.8395 at A_e/A_o = 0.3125, before subsequently declining down to σ_U/σ_M = 0.4817 at A_e/A_o = 0.5625 **(Fig. 2c)**. We also examined the impact of varying the charge input Q at a fixed A_e/A_o = 0.4375, and observed that, at a low charge input, Q = 200 mAh, σ_U/σ_M = 0.6244 but as Q is increased to 400 mAh and beyond, σ_U/σ_M reached and remained around 1.0 **(Fig. 2d)**.

To develop a quantitative model of these experiments, we first differentiated samples by the type of fracture experienced upon post-healing tensile testing. Three types of fracture were observed: I, P, and M **(Fig. 2e)**. In type I, de-bonding occurred at the interface between the plated nickel and the structural metal, with the metal sliding out of the plated nickel sleeve that surrounds it. In type P, the plated nickel fractured at the same location as the initial fracture. In type M, the metal dogbone fractured in a new location, indicating that the tensile strength of the healed sample was approximately equal to the tensile strength of a pristine sample. The incidence of these three types of fracture varied with changes in A_e **(Fig. 2f)**. Samples healed with Q = 1000 mAh all experienced type-I fracture at low A_e/A_o, but as A_e increased, the incidence of type-M fracture increased at the expense of type-I fracture. Samples healed with Q = 200 mAh experienced the same high incidence of type-I fracture at low A_e, though unlike 1000 mAh samples, the incidence of type-P fracture increased with larger A_e. Comparing the data in **Fig. 2c** and **Fig. 2f** reveals that type-I fracture was always dominant at low A_e/A_o, type-M fracture was prevalent when $\sigma_U/\sigma_M \sim 1$, while an increasing prevalence of type-P fracture was associated with declining σ_U/σ_M.

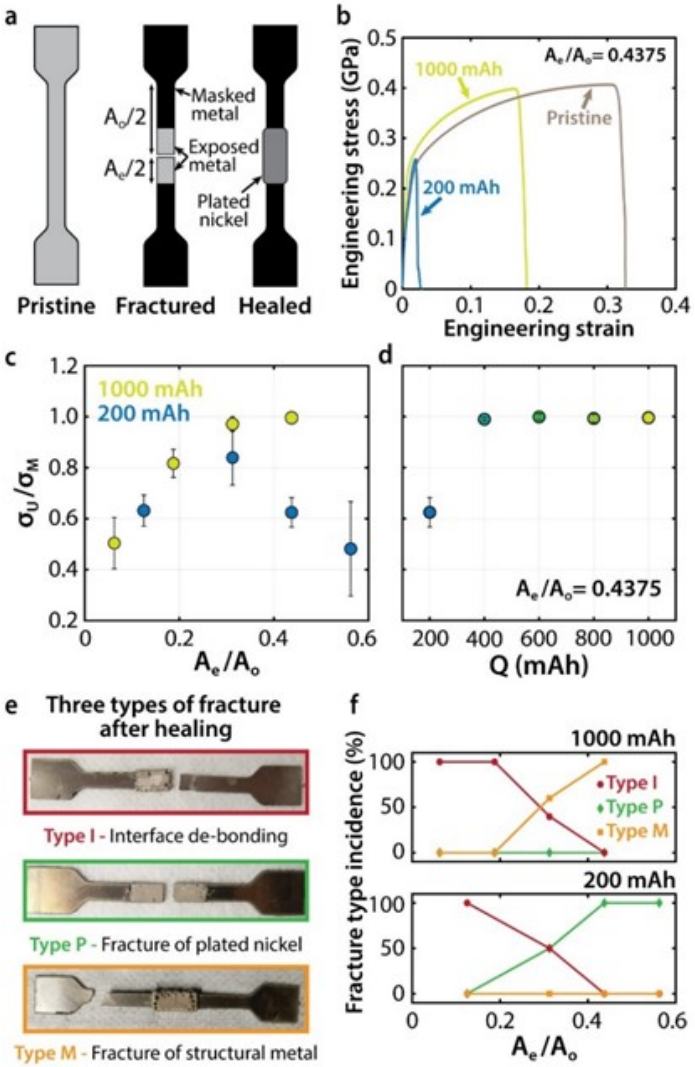

Fig 2. Electrochemical healing of a nickel alloy. (a) Illustrations of Ni 200 dogbone samples in the pristine, fractured, and healed state. The fractured sample is masked to leave only an area A_e exposed. (b) Stress-strain data of a pristine Ni200 sample, and two samples with the same exposed area, healed with different charge inputs (200 and 1000 mAh). (c) Strength healing efficiency σ_U/σ_M as a function of exposed area ratio A_e/A_o for Ni 200 samples healed using a charge input of 200 mAh and 1000 mAh. (d) Strength healing efficiency σ_U/σ_M as a function of charge input Q for Ni 200 samples with A_e/A_o = 0.4375. (e) Photographs showing the three types of fracture sustained by healed samples upon subsequent tensile loading. (f) Incidence of the three types of fracture after healing as function of A_e/A_o in Ni 200 samples healed with 1000 mAh and 200 mAh of charge input. Each datapoint corresponds to between 3 and 5 samples.

Informed by these experimental insights, we developed a model that predicts the tensile strength of healed samples for each type of fracture. Assuming force continuity and using Faraday's law, we related σ_U (the tensile strength of the healed sample) to τ_{Ni-M} (the interfacial shear strength, for type-I fracture), σ_M (the tensile strength of the structural metal, for type-M fracture), and σ_{Ni} (the tensile strength of plated nickel, for type-P fracture)

through a single independent variable $X = A_e/A_M$, where A_M is the cross-sectional area of the structural metal. The three governing equations of the model are

$$\sigma_U = \sigma_{Ni}\frac{A_{Ni}}{A_M} = 2\sigma_{Ni}\left(\frac{1}{A_M}\right)^3\left(\frac{\varepsilon QM}{2F\rho}\right)\left(2\left(\frac{\varepsilon QM}{2F\rho}\right)X^{-2} + A_M(L_M + W_M)X^{-1}\right) \quad (1)$$

for type-P fracture,

$$\sigma_U = \tau_{Ni-M}X + \sigma_{Ni-M,o} \quad (2)$$

for type-I fracture, and

$$\sigma_U = \sigma_M \quad (3)$$

for type-M fracture, where A_{Ni} is the cross-sectional area of plated nickel, ε is the cathodic efficiency of nickel plating **(Table S1)**, M is the molar mass of nickel (58.69 g/mol), F is Faraday's constant (96,485 C/mol), and ρ is the mass density of nickel (8,900 kg/m^3), L_M and W_M are the thickness and width of the structural metal such that $A_M = L_M W_M$, and $\sigma_{Ni-M,o}$ is an added stress term. The theoretical model is described in greater detail in the ***Supporting Information***.

Figure 3a shows σ_U/σ_M as a function of A_e/A_M for each fracture type using expressions (1), (2), and (3). For a given value of A_e/A_M, the lowest curve determines the type of fracture that occurs and the achievable strength healing efficiency σ_U/σ_M. There are two hypothetical healing cases. In case 1, the type-I line intersects the type-P curve below the sample's pristine strength (type-M horizontal line), which means that $\sigma_U/\sigma_M = 1$ cannot be achieved and full recovery of tensile strength is not possible. In case 2, the intersection point moves above the type-M line, either due to the use of plated metal with a higher tensile strength, an increase in the charge input, or an increase in the interfacial shear strength. This opens a window in which $\sigma_U/\sigma_M = 1$, or full healing, is physically possible.

This model showed good agreement with the healed Ni 200 samples **(Fig. 3b, Table S4)**. A linear regression of the type-I fracture line showed that $\tau_{Ni-M} = 6.14\,MPa$ and $\sigma_{Ni-M,o} = 158.97\,MPa$ **(Fig 3b, red line; Fig. S14)**. Since we used no chemical or electrochemical treatment before nickel plating to maintain a simple healing process, the Ni-metal interface shear strength, τ_{Ni-M}, was lower than values reported from ring shear tests of nickel plated on different metals, including nickel itself [45,47]. Type-P fracture curves were plotted for charge inputs from 200 to 1000 mAh, with the tensile strength of plated nickel at $\sigma_{Ni} = 358\,MPa$ **(Fig. S5)**. Experimental data and type-P fracture curves are colored in shades of green according to the charge input used **(Fig. 3b)**. The type-P fracture curve for 200 mAh is slightly above, but closely follows experimental data for samples healed with 200 mAh and A_e/A_M values of 41.36, 57.91, and 74.45. The experimental data from **Fig. 2d** is also shown in **Fig. 3b**, with a cluster of datapoints at $\sigma_U/\sigma_M \sim 1.0$ and $A_e/A_M = 57.91$. **Fig. 3b** demonstrates that to guarantee full healing, or $\sigma_U/\sigma_M \sim 1.0$, two conditions need to be met: a sufficiently high exposed area so that $A_e/A_M > 45$, and a charge input higher than 200 mAh.

Interestingly, the samples retained significant strength, $\sigma_U/\sigma_M \sim 0.4$, when there was no exposed metal on which nickel could be plated, $A_e/A_M = 0$. To explain this, we compared the surface morphologies of the cross-sections of a pristine sample **(Fig. 3c, d)** and a healed

sample after type-P fracture **(Fig. 3e, f)**. The pristine sample cross-section shows plastic damage resulting from waterjet cutting, while the healed sample cross-section shows clear morphological evidence of plated nickel suggesting that there was a microscale gap which allowed nickel ion transport, and thus, nickel deposition and adhesion at the cross-sectional areas. As a result, we expect a non-zero tensile strength in healed samples even if A_e = 0, which we accounted for in the model with the $\sigma_{Ni-M,o}$ stress term **(equation 2)**.

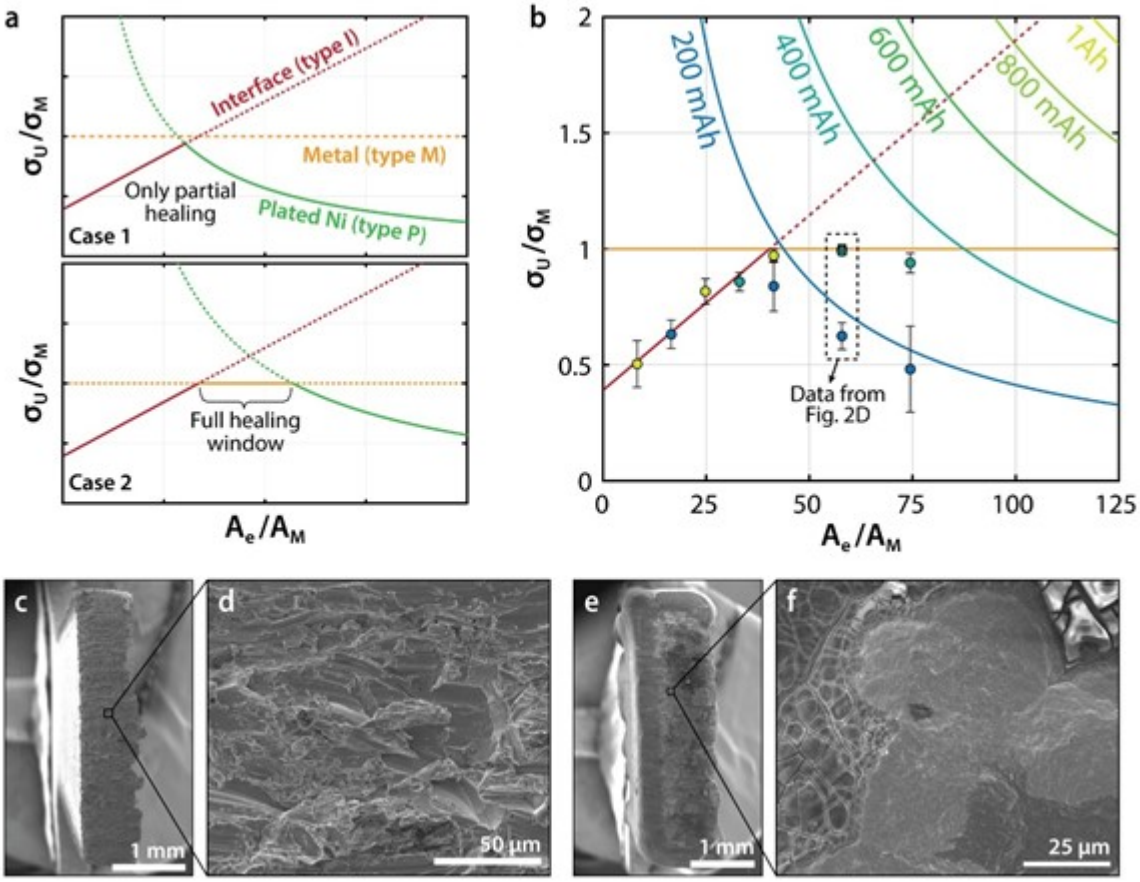

Fig 3. Model for effective tensile strength recovery. (a) Two plots of σ_U/σ_M as a function of A_e/A_M that include three curves corresponding to each fracture type (I, P, M). The top plot represents a hypothetical case in which only partial healing is possible (σ_U/σ_M <1), while the bottom plot represents a case in which full healing (σ_U/σ_M =1) is possible. (b) Plot of σ_U/σ_M as a function of A_e/A_M showing the theoretical model applied to healed nickel (Ni 200) samples. The circles with standard deviation bars are experimental data, with circles colored according to the corresponding charge input. The data enclosed by the dashed line rectangle is the same data shown in Fig. 2d. (c) SEM image of cross-section of half-dogbone Ni 200 sample. (d) Higher magnification image of (c) showing detail of surface morphology. (e) SEM image of cross-section of Ni 200 sample after post-healing type-P fracture. (f) Higher magnification image of (e) showing the presence of plated nickel within the cross-sectional area.

Extending our framework to various types of structural metals demonstrated the viability of electrochemical healing as an alternative to conventional welding. With the same experimental approach used with Ni 200 samples, we electrochemically healed low-carbon steel (AISI 1008), and two "unweldable" aluminum alloys (Al 2024 and Al 7075). In **Fig. 4a**, we applied the theoretical model to AISI 1008 samples healed with 400 and 800 mAh of charge input. Linear regression of the type-I fracture line showed that $\tau_{Ni-M} = 7.61\ MPa$ **(Fig 4a, red line; Fig. S14)**. Fitting the type-P curve to experimental data revealed that $\sigma_{Ni} = 213.4\ MPa$, which is lower than expected likely due to the presence of iron within plated nickel **(Fig. S17)**. Using 800 mAh of charge input, healing at $A_e/A_M = 74.45$ and $A_e/A_M = 91.00$ resulted in full restoration of tensile strength, with strength healing efficiencies σ_U/σ_M of 1.010 and 1.022 respectively. In **Fig. 4b**, we applied our theoretical model to Al 7075 samples healed with 200 and 400 mAh. Linear regression of the type-I fracture line showed that $\tau_{Ni-M} = 7.23\ MPa$ and $\sigma_{Ni-M,o} = 97.10\ MPa$ **(Fig 4b, red line; Fig. S14)**. Fitting the type-P curve to experimental data revealed that $\sigma_{Ni} = 387.42\ MPa$, which is close to the measured value of 358.2 MPa **(Fig. S5)**. Using 400 mAh of charge input, full healing of tensile strength was achieved at $A_e/A_M = 63.00$ and $A_e/A_M = 81.00$, indicated by strength healing efficiencies σ_U/σ_M of 1.022 and 1.021 **(Fig. 4b, Table S6)**. In **Fig. 4c**, we applied the theoretical model to Al 2024 samples healed with 400 and 600 mAh. Linear regression showed that $\tau_{Ni-M} = 6.65\ MPa$ and $\sigma_{Ni-M,o} = 4.44\ MPa$ **(Fig 4c, red line; Fig. S14)**. Fitting the type-P curve to experimental data revealed that $\sigma_{Ni} = 330.88\ MPa$, which is close to the measured value of 358.2 MPa **(Fig. S5)**. As a charge input of 400 mAh was insufficient to enable full healing, we healed Al 2024 samples with 600 mAh of charge input at $A_e/A_M = 81.00$ and $A_e/A_M = 99.00$, achieving near-full healing with σ_U/σ_M at 0.9532 and 0.9574 respectively **(Fig. 4c, Table S7)**. Occasional stress concentration at the junction between the plated area and the non-plated area led to a substantial reduction in strength recovery at $A_e/A_M = 99.00$, from $\sigma_U/\sigma_M = 0.9574$ to $\sigma_U/\sigma_M = 0.7153$ (downward arrow in **Fig. 4c**).

Remarkably, the ability of this electrochemical healing framework to fully restore tensile strength in fractured metals was insensitive to nickel-metal adhesion. Shear strengths at the interface between plated nickel and the four healed metals (Ni 200, AISI 1008, Al 2024, and Al 7075) ranged between 6.1 and 7.6 MPa **(Fig. S14)**. These values are very low compared to 10x to 70x higher interfacial shear strength values measured via ring shear testing of nickel plated on a range of metallic alloys, which underwent multi-step processes that included chemical or electrochemical pre-treatment in acidic solutions, followed in some cases by plating in a low-pH nickel solution (e.g., Woods strike), before plating in a standard nickel sulfamate solution [45,47,51]. Our framework obviates the need for these multi-step processes since it removes interfacial adhesion as the limiting factor of healing performance, replacing it instead with factors that can more easily be controlled such as exposed area and charge input.

Healing waterjet-cut metal samples validated the theoretical model and demonstrated effective restoration of tensile strength. However, our framework could also heal metals that were plastically deformed and fractured under tensile loading. AISI 1008 steel dogbone

samples were fully fractured in tension, then healed to recover ~100 % of pristine tensile strength. Mechanical polishing of the fracture surface reduced the requirements of full healing in terms of charge input (from 1600 mAh to 1000 mAh) and time (from 50 hours to 16 hours) (see the ***Supporting Information***, **Fig. S18**).

Though our framework targets tensile strength recovery in fractured metals, it suggests the possibility of full recovery of both toughness and tensile strength under specific conditions. Here, toughness, which is also known as "work of fracture", refers to the area under the stress-strain curve. Similar to Ni 200 samples, type-I fracture dominated initially in Al 2024 and Al 7075, before declining in favor of type-P and type-M fractures **(Fig. 4d)**. For Al 2024, the incidence of type-I fracture decreased to 0 % at $A_e/A_M = 81$, as the incidences of type-M and type-P fractures increased to 40 % and 60 %, respectively. Incidence of type-P fracture then increased further in line with our theoretical prediction that type-P fracture dominates for large A_e/A_M. For Al 7075, type-M and type-I fractures co-existed while A_e/A_M was between 45 and 81, but as A_e/A_M increased to 99, type-P fracture dominated. The co-existence of type-M and type-I fracture within this intermediate range of A_e/A_M values occurred along with high toughness recovery, in addition to full recovery of tensile strength. **Fig. 4e** shows the stress-strain data of four Al 7075 samples healed with Q = 400 mAh and A_e/A_M = 81, with two experiencing type-I fracture and the two others experiencing type-M fracture. While all four samples exhibited similar tensile strength with $\sigma_U/\sigma_M \sim 1$, the samples that experienced type-I fracture showed remarkably high toughness (area under the stress-strain curve) as the plated nickel slid across the Al 7075 surface during loading. Toughness healing efficiency U/U_M, the ratio of healed to pristine toughness, for all Al 7075 samples rose with increasing A_e/A_M, peaked at $U/U_M = 1.00$ for $A_e/A_M = 63$, then decreased to $U/U_M = 0.258$ for $A_e/A_M = 99$ **(Fig. 4f, yellow data)**. Toughness healing efficiency was highest for samples that experienced type-I fracture, peaking at $U/U_M = 1.364$ for $A_e/A_M = 81$ **(Fig. 4f, red data; Table S8)**. In summary, healed Al 7075 samples with A_e/A_M values equal to or slightly higher than the A_e/A_M at which the type-I and type-M fracture lines intersect (red and yellow lines in **Fig. 4b**) were likely to experience type-I fracture, and as a result, to exhibit up to 136% recovery of toughness (or work of fracture). This insight opens the door to future developments that may enable improved toughness recovery in healed metals under tensile loading.

In addition to repairing "unweldable" alloys, electrochemical healing enabled tensile strength recovery in 3D printed metal structures with complex geometries, which would be impossible to repair using conventional welding. Using 3D/polyhedral graphic statics as a design method and selective laser melting of AlSi10Mg for 3D printing, we fabricated a funicular shellular structure that carries internal forces axially (no transverse stress) **(Fig. S12)** and is designed to fail at its central section, which includes three outer struts and a middle strut that is difficult to access **(Figs. 5a, S4)**. This structure is a type of funicular polyhedral frame designed using a technique of topological subdivision which generates two-manifold anticlastic surface-based structures with cross-sections normal to the direction of the internal force flow for any given loading condition [52–55] (see ***Supporting Information***).

Owing to its geometric complexity and the inaccessibility of the middle strut, this structure could not be repaired by conventional welding and would need to be re-printed or replaced. We loaded the structure in tension until the four struts fractured, healed it via selective nickel plating, then fractured it in tension again to assess the recovery of tensile strength **(Fig. 5b)**. In addition to the healing process which we have used thus far (potentiostatic plating at -1.8V vs. Ni), we used an enhanced process in which we apply 1000 cycles of pulsed plating (one cycle includes plating at -1.8V vs. Ni for 5 seconds followed by -0.2V vs. Ni for 3 seconds) before proceeding with potentiostatic plating at -1.8V vs. Ni **(Fig. S13)**. We have shown in an earlier work that pulsed plating mitigates diffusion-limited electrodeposition, which improves nickel adhesion to the healed metals and prevents void formation at the fracture gaps [41]. The normal healing process (potentiostatic only) with Q = 1200 mAh resulted a low 38.5 % recovery of tensile strength **(top plot in Fig. 5c, Fig. S13 A)**, while the enhanced healing process (pulsed + potentiostatic) with Q = 1200 mAh enabled a 110.1 % recovery of tensile strength **(bottom plot in Fig. 5c Fig. S13 B)**. We observed that the normal healing process resulted in type-P fracture of all four struts, while the enhanced process resulted in type-P fracture at the central strut, with limited or no type-I fracture at the three outer struts **(Fig. 5b, S13)**. By maximizing nickel density at the fracture gap, this enhanced process can be attractive in cases where there are constraints either on energy (e.g., battery-powered robot) or on metal area available for plating.

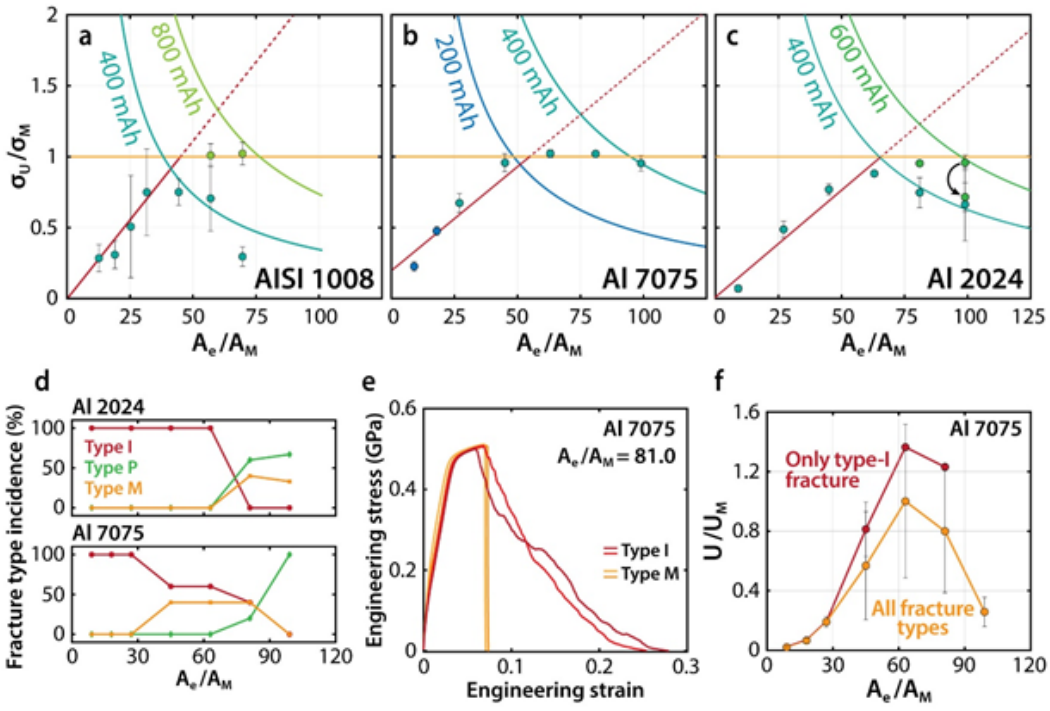

Fig 4. Electrochemical healing of steel and "unweldable" aluminum alloys. (a) Plot of σ_U/σ_M as a function of A_e/A_M showing the model applied to healed AISI 1008 steel samples. The circles with standard deviation bars represent experimental data, with circles colored according to the corresponding charge input. (b) Plot of σ_U/σ_M as a function of A_e/A_M showing the model applied to

healed Al 7075 samples. (c) Plot of σ_U/σ_M as a function of A_e/A_M showing the model applied to healed Al 2024 samples. (d) Incidence of the three types of fracture after healing as function of A_e/A_M for healed Al 2024 and Al 7075 samples (Al 2024 samples healed with 600 mAh are excluded). (e) Strain-strain data of four healed Al 7075 samples with A_e/A_M = 81.0 that experienced type-I and type-M fracture. (f) Plot of toughness healing efficiency *U/Um* for healed Al 7075 samples with respect to A_e/A_M. Yellow data corresponds to all Al 7075 samples, while red data corresponds only to samples that experienced type-I fracture.

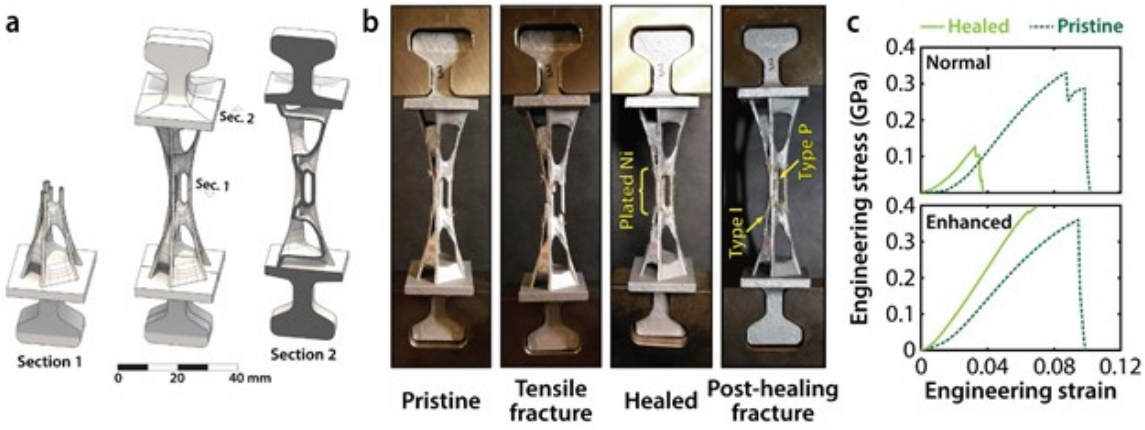

Fig 5. Electrochemical healing of a 3D printed shellular funicular structure. (a) Rendering of the shellular structure with vertical and horizontal sections. (b) Photographs of a 3D printed shellular structure in its pristine state, after initial tensile fracture, after healing, and after post-healing fracture. (c) Pristine and healed stress-strain data for two shellular structures, one healed with the normal process (potentiostatic only), and another healed with the enhanced process (pulsed + potentiostatic).

Using electrochemical healing to repair metals in practical applications requires careful consideration of its energetic, financial, and time requirements across length scales. We used our model (with properties for Al 7075) to estimate the charge input, Q **(Fig. 6a)**, financial cost, C **(Fig. 6b)**, and time, T **(Fig. 6c)** required for full healing in fractured metals with a cross-sectional area ranging from 10^{-8} to 1 m^2. For metals similar in size to the dogbone samples in this study (A_M = 2.0 mm^2), full healing would require 335 mAh, 30 hours, and \$0.01. Q and C are low, if not negligible, for small length scales, but rise at an increasing rate as length scale increases. On the other hand, T rises with a declining rate as length scale increases but may become prohibitively high at large length scales. See the ***Supporting Information*** for the full derivation of Q, C, and T **(Eqs. S17-S22)**. Improving the adhesion between the plated nickel and structural metal, as measured by the interfacial shear strength τ_{Ni-M}, using proven chemical and electrochemical processes [41,45,47], can decrease the energetic and financial costs of electrochemical healing. For a structural metal with A_M = 2.0 mm^2, required charge input decreases by 80% to 67.1 mAh due to a 5x improvement in τ_{Ni-M}, by 90% to 33.5 mAh due to a 10x improvement, and by 95% to 16.8 mAh due to a 20x improvement. Thus, the marginal benefit of improving τ_{Ni-M} declines rapidly, which suggests that common electrochemical pretreatments [41] might be the optimal choice. Though we focused our cost-reduction analysis on increasing interfacial shear strength, τ_{Ni-M}, using

plated metal with higher tensile strength or increasing the average current density during plating would also lower the costs of full healing.

According to the scaling relationships that govern Q, C, and T **(Figs. 6a–c)**, with $\tau_{Ni-M} = 7.23\,MPa$, healing a standard concrete-reinforcing steel bar or a metal part of similar size ($A_M \sim 10^{-4}$ m^2), would require \$4.0, 224 hours (or 9.3 days), and 123 Ah (or 0.3 % of the capacity of a Tesla Model 3 battery at 1.8 V) [56]. A 100 mA/cm^2 current density would reduce the healing time tenfold, to 22.4 hours. Costs increase dramatically for a large metal part ($A_M \sim 0.1$ m^2): \$125,892, 7079 hours (or 9.7 months), and 3,890,451 Ah (or 93x the capacity of a Tesla Model 3 battery at 1.8 V) [56], where financial cost is dominated by nickel. In summary, without the implementation of cost reduction measures, electrochemical healing is attractive for metal fractures from the micrometer to the centimeter-scale, but can be prohibitively expensive and slow at or near the meter-scale.

With these scaling relationships in mind, we used electrochemical healing to repair a fully fractured ¼-inch chrome-coated steel wrench, with cross-sectional area $A_M \sim 30$ mm^2 **(Fig. 6d)**. We applied a total charge input of 8,230 mAh over 138 hours in an unstirred room temperature bath **(Fig. 6e, f)**. The wrench recovered a functional level of bending strength and withstood multiple loadings at torques up to 10 N.m, with no discernable damage (**Fig. 6g**, see video in the ***Supporting Information***). Therefore, the healed wrench could readily meet the 3.6 N.m minimum tightening torque for ¼ inch ASTM A307 bolts and 8.5 N.m minimum tightening torque for ¼ inch SAE J429 Grade 5 bolts, which are used in a range of industrial applications [57]. Healing a wrench demonstrated the recovery of functionality after full fracture of a common metallic part. With further electrolyte and process optimization [41], faster and stronger electrochemical healing could be deployed as an effective approach to repair many high-value metallic parts.

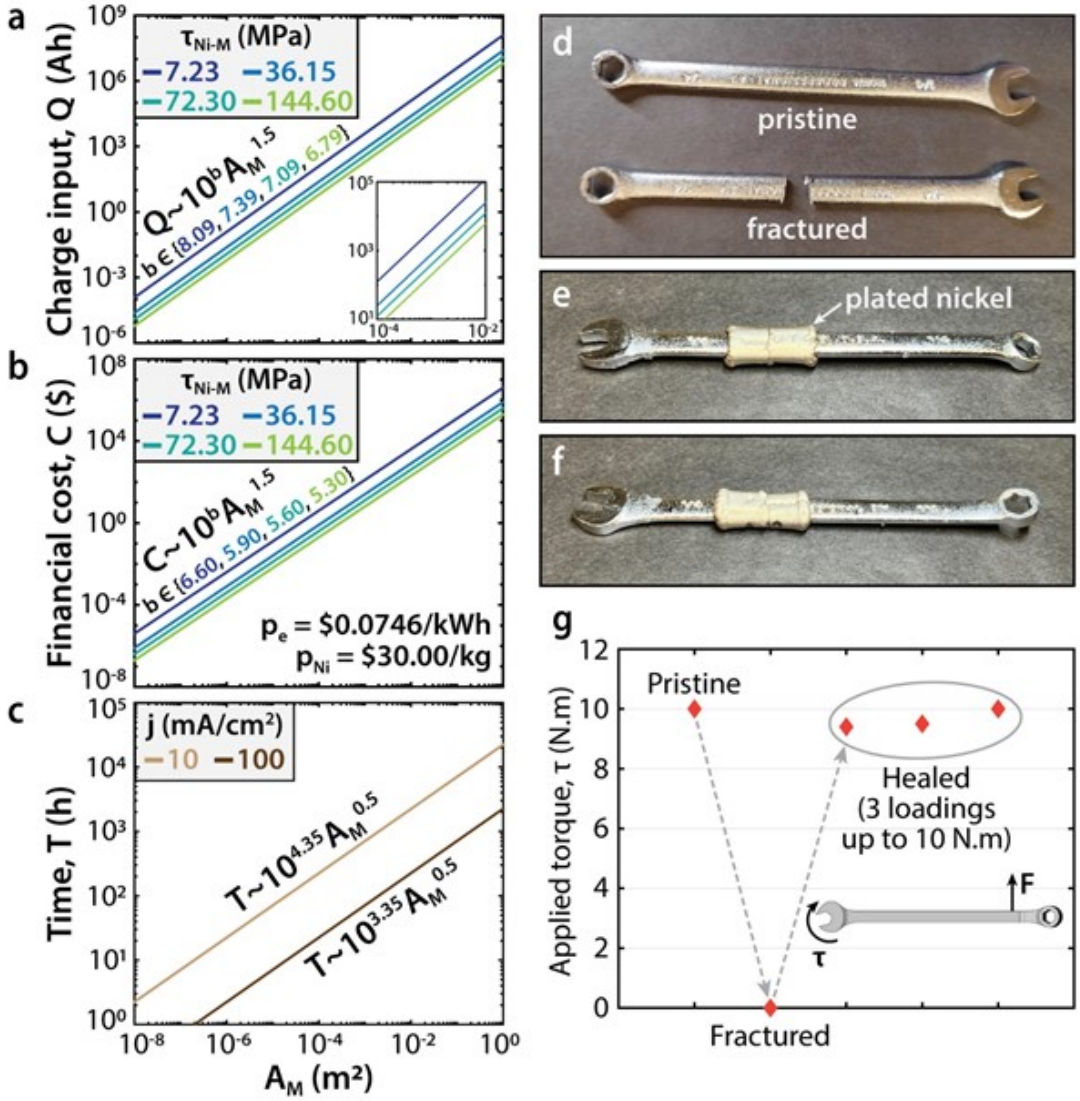

Fig 6. Practical application of electrochemical healing at different length scales. (a) Minimum charge input required for full healing for metals with a cross-sectional area A_M ranging from 10^{-8} to 1 m^2 assuming 1x, 5x, 10x, and 20x improvement in shear strength at the nickel-metal interface, including inset showing data for A_M ranging from 10^{-4} to 10^{-2} m^2. (b) Financial cost of healing due to the consumption of electricity and nickel, assuming 1x, 5x, 10x, and 20x improvement in shear strength at the nickel-metal interface. (c) Time required for full healing with a current density of 10 mA/cm^2. (d) Pristine and fractured chrome-coated steel wrench. (e,f) Both sides of a fractured wrench after healing with 8,200 mAh. (g) Torque applied to a pristine, fractured, and healed wrench after loading with a 10 N.m torque wrench.

Conclusion

Room-temperature electrochemical healing represents a radical shift from the current high temperature approaches to repair metals, including welding. We presented a framework for the effective electrochemical healing of fractured metals based on a model that relates the recovery of tensile strength to relevant geometric (e.g., exposed area, cross-sectional area), electrochemical (e.g., charge input, cathodic efficiency), and mechanical parameters. We experimentally validated this model and demonstrated full recovery of tensile strength in a nickel alloy, low-carbon steel, and two "unweldable" aluminum alloys. We also showed that fully recovering both toughness and tensile strength is possible under specific conditions. Informed by this framework and using a healing process that combined pulsed and potentiostatic plating, we enabled full restoration of tensile strength in a 3D printed difficult-to-weld shellular structure. Repairing 3D printed parts mitigates the high energy and cost associated with the current approach of recycling and reprinting fractured parts. To facilitate the adoption of electrochemical healing, we revealed the scaling relationships that govern the charge input, financial cost, and time required for full healing at different length scales, as well as demonstrated the restoration of a functional level of strength in a fractured wrench.

In short, this work enables 100 % recovery of tensile strength in a diverse range of metallic materials using a simple nickel sulfamate electrolyte; a well-studied, widely-used, and relatively inexpensive electrolyte chemistry, which could potentially enable a universal and scalable approach to repair fractured metals at various length scales. Electrochemical healing could also open exciting possibilities such as electrically-controlled autonomous and preemptive repair [40], as well as enable 3D-printed metal structures optimized for repair through funicularity and designed failure characteristics. Electrochemical healing could reduce demand for metal mining and refining, thus mitigating the emissions intensity of structural metals by up to 400 kg of CO_2 per ton of metal [9], and moving us forward on the road to sustainability and net-zero emissions. Future work could improve the healing time with convective flow of the electrolyte, increase the adhesion strength of electrodeposited metals, and reduce cost with alternative electrodeposited metals.

Materials and Methods

A detailed description of the materials and methods used in this study can be found in the ***Supporting Information***, including details on (i) electrolyte chemistry, (ii) preparation of dogbone samples, (iii) design and 3D printing of the shellular funicular structure, (iv) electrochemical healing methods, (v) mechanical testing, (vi) preparation and testing of free-standing plated nickel, and (vii) materials characterization. The ***Supporting Information*** also includes details on the theoretical model and extensive experimental data.

Data and materials availability

All data needed to evaluate the conclusions of this study are available in the article or Supporting Information. Additional data may be obtained from the authors upon reasonable request.

Contributions

Z.H. and J.H.P. designed research; Z.H. performed experiments, with assistance from A.P. and Z.J.; Z.H. developed the theoretical model, with assistance from Z.J.; M. Akbari designed the shellular structure; J.H.P. and M. Akbarzadeh supervised research; and Z.H. wrote the article with contributions from M. Akbari, M. Akbarzadeh, and J.H.P.

Competing Interests

J.H.P and Z.H. are inventors on a pending patent application (U.S. 17/291,657) which encompasses at least part of the work discussed in this article.

Acknowledgements

We thank Jeremy Wang for waterjet cutting, Jason Pastor and Peter Szczesniak for the fabrication of tension grips, Yichao Shi for assistance with photography, and Alissa Johnson for assistance with XRD. We thank Gnana Saurya Vankayalapati and Prof. Kevin Turner for graciously providing access to a mechanical testing tool used for some preliminary testing, and Xiaoheng Zhu, Chengyang Mo, and Prof. Jordan Raney for providing access to an Instron 68SC-5 mechanical testing tool.

This work was performed in part at the Singh Center for Nanotechnology, a node in the National Nanotechnology Coordinated Infrastructure (NNCI) network, which is supported by the National Science Foundation under grant NNCI-1542153. J.H.P acknowledges funding from the TMS Foundation (Early Career Faculty Fellow Award) and the U.S. Air Force Office of Scientific Research (grant no. FA9550-22-1-0095). M. Akbarzadeh acknowledges funding from the National Science Foundation through a CAREER Award (CAREER-1944691-CMMI) and a Future Eco Manufacturing Research Grant (FMRG-CMMI 2037097).

References

[1] T. Vass, P. Levi, A. Gouy, H. Mandová, *Iron and Steel*, Paris, **2021**.

[2] International Aluminum Institute, "Statistics," can be found under https://international-aluminium.org/statistics/, **2021**.

[3] World Steel Association, "Total production of crude steel," can be found under https://worldsteel.org/steel-by-topic/statistics/annual-production-steel-data, **2022**.

[4] D. Raabe, C. C. Tasan, E. A. Olivetti, *Nature* **2019**, *575*, 64.

[5] W. R. Stahel, *Nature* **2016**, *531*, 435.

[6] J. Rockström, W. Steffen, K. Noone, Å. Persson, F. S. Chapin, E. F. Lambin, T. M. Lenton, M. Scheffer, C. Folke, H. J. Schellnhuber, B. Nykvist, C. A. de Wit, T.

Hughes, S. van der Leeuw, H. Rodhe, S. Sörlin, P. K. Snyder, R. Costanza, U. Svedin, M. Falkenmark, L. Karlberg, R. W. Corell, V. J. Fabry, J. Hansen, B. Walker, D. Liverman, K. Richardson, P. Crutzen, J. A. Foley, *Nature* **2009**, *461*, 472.

[7] J. N. Moore, S. N. Luoma, *Environ. Sci. Technol.* **1990**, *24*, 1278.

[8] International Aluminum Institute, "Global Aluminum Cycle 2019," can be found under https://alucycle.international-aluminium.org/public-access/, **2021**.

[9] K. Daehn, R. Basuhi, J. Gregory, M. Berlinger, V. Somjit, E. A. Olivetti, *Nat. Rev. Mater.* **2022**, *7*, 275.

[10] C. H. Cadden, *Encycl. Mater. Sci. Technol.* **2006**.

[11] K. Weman, *Welding Processes Handbook*, CRC Press, Boca Raton, FL, **2003**.

[12] E. R. Caley, *J. Chem. Educ.* **1926**, *3*, 1149.

[13] A. Hosoi, T. Nagahama, Y. Ju, *Mater. Sci. Eng. A* **2012**, *533*, 38.

[14] H. Song, Z. J. Wang, X. D. He, J. Duan, *Sci. Rep.* **2017**, *7*, 1.

[15] V. Kilicli, X. Yan, N. Salowitz, P. K. Rohatgi, *Jom* **2018**, *70*, 846.

[16] J. Martinez Lucci, R. S. Amano, P. Rohatgi, B. Schultz, in *ASME Int. Mech. Eng. Congr. Expo.*, ASME, **2008**, pp. 1759–1768.

[17] I. M. Van Meerbeek, B. C. Mac Murray, J. W. Kim, S. S. Robinson, P. X. Zou, M. N. Silberstein, R. F. Shepherd, *Adv. Mater.* **2016**, *28*, 2801.

[18] S. Zhang, C. Kwakernaak, W. Sloof, E. Brück, S. Van Der Zwaag, N. Van Dijk, *Adv. Eng. Mater.* **2015**, *17*, 598.

[19] N. H. van Dijk, S. van der Zwaag, *Adv. Mater. Interfaces* **2018**, *1800226*, 1.

[20] J. T. Kim, H. J. Kim, S. H. Hong, H. J. Park, Y. S. Kim, Y. J. Hwang, Y. B. Jeong, J. Y. Park, J. M. Park, B. Sarac, W. M. Wang, J. Eckert, K. B. Kim, *Sci. Rep.* **2018**, *8*, 2.

[21] S. Danzi, V. Schnabel, J. Gabl, A. Sologubenko, H. Galinski, R. Spolenak, *Adv. Mater. Technol.* **2019**, *4*, 1.

[22] M. Sokoluk, C. Cao, S. Pan, X. Li, *Nat. Commun.* **2019**, *10*, 1.

[23] M. Sheikhi, F. Malek Ghaini, H. Assadi, *Acta Mater.* **2015**, *82*, 491.

[24] S. Catchpole-Smith, N. Aboulkhair, L. Parry, C. Tuck, I. A. Ashcroft, A. Clare, *Addit. Manuf.* **2017**, *15*, 113.

[25] G. Çam, G. İpekoğlu, *Int. J. Adv. Manuf. Technol.* **2017**, *91*, 1851.

[26] H. Cerjak, Ed. , *Mathematical Modelling of Weld Phenomena 6*, Maney Publishing, London, **2002**.

[27] K. Nakata, Y. G. Kim, M. Ushio, T. Hashimoto, S. Jyogan, *ISIJ Int.* **2000**, *40*, DOI 10.2355/isijinternational.40.suppl_s15.

[28] R. J. Stueber, T. Milidantri, M. Tadayon, *Welding High-Strength Nickel Superalloys*, **1994**, US 5,374,319.

[29] M. Osanov, J. K. Guest, *Annu. Rev. Mater. Res.* **2016**, *46*, 211.

[30] M. Akbarzadeh, 3D Graphical Statics Using Reciprocal Polyhedral Diagrams, ETH Zurich, **2016**.

[31] J. J. Lewandowski, M. Seifi, *Annu. Rev. Mater. Res.* **2016**, *46*, 151.

[32] H. Canaday, *Aerosp. Am.* **2018**.

[33] S. Das, D. L. Bourell, S. S. Babu, *MRS Bull.* **2016**, *41*, 729.

[34] J. H. Martin, B. D. Yahata, J. M. Hundley, J. A. Mayer, T. A. Schaedler, T. M. Pollock, *Nature* **2017**, *549*, 365.

[35] A. Mortensen, J. Llorca, *Annu. Rev. Mater. Res.* **2010**, *40*, 243.

[36] W. Shan, T. Lu, C. Majidi, *Smart Mater. Struct.* **2013**, *22*, DOI 10.1088/0964-1726/22/8/085005.

[37] M. Kaur, T. H. Kim, W. S. Kim, *Adv. Mater.* **2021**, *33*, DOI 10.1002/adma.202002534.

[38] C. Semini, J. Goldsmith, D. Manfredi, F. Calignano, E. P. Ambrosio, J. Pakkanen, D. G. Caldwell, in *Proc. 17th Int. Conf. Adv. Robot.*, IEEE, **2015**, pp. 123–129.

[39] F. Hussain, R. Goecke, M. Mohammadian, *Proc. Inst. Mech. Eng. Part H J. Eng. Med.* **2021**, *235*, 1375.

[40] Z. Hsain, J. H. Pikul, *Adv. Funct. Mater.* **2019**, *29*, DOI 10.1002/adfm.201905631.

[41] Z. Hsain, Z. Jiang, J. H. Pikul, *Multifunct. Mater.* **2021**, *4*.

[42] X. G. Zheng, Y. N. Shi, K. Lu, *Mater. Sci. Eng. A* **2013**, *561*, 52.

[43] X. G. Zheng, Y.-N. Shi, K. Lu, *J. Electrochem. Soc.* **2016**, *163*, D349.

[44] X. G. Zheng, Y.-N. Shi, K. Lu, *J. Electrochem. Soc.* **2013**, *160*, D289.

[45] J. W. Dini, H. R. Johnson, *Surf. Technol.* **1977**, *5*, DOI 10.1016/0376-4583(77)90063-2.

[46] H. R. Johnson, J. W. Dini, *Rev. Sci. Instrum.* **1975**, *46*, 109.

[47] J. W. Dini, H. R. Johnson, *Plating on Some Difficult-to-Plate Metals and Alloys*, Livermore, CA, **1980**.

[48] G. Sheela, C. R. Rao, S. S. Azim, K. Kumar, M. Pushpavanam, *Trans. Inst. Met. Finish.* **2004**, *82*, 24.

[49] J. W. Dini, H. R. Johnson, *Met. Eng. Q.* **1974**, *14*, 6.

[50] D. Taylor, J. G. Hazenberg, T. C. Lee, *Nat. Mater.* **2007**, *6*, 263.

[51] J. W. Dini, W. K. Kelley, H. R. Johnson, in *Test. Met. Inorg. Coatin* (Eds.: W.B. Harding, G.A. Di Bari), ASTM, Philadelphia, **1987**.

[52] M. Akbari, M. Akbarzadeh, M. Bolhassani, in *Proc. IASS Annu. Symp. 2019 - Struct. Membr.*, **2019**.

[53] M. Akbari, A. Mirabolghasemi, H. Akbarzadeh, M. Akbarzadeh, in *Symp. Comput. Fabr.*, **2020**, pp. 1–11.

[54] M. Akbari, Y. Lu, M. Akbarzadeh, *Proc. Assoc. Comput. Des. Archit.* **2021**.

[55] M. Akbari, A. Mirabolghasemi, M. Bolhassani, A. Akbarzadeh, M. Akbarzadeh, *Adv. Funct. Mater.* **2022**, *2109725*, 1.

[56] "Tesla Model 3 Long Range Dual Motor," can be found under https://ev-database.org/car/1591/Tesla-Model-3-Long-Range-Dual-Motor, **2022**.

[57] "Torque-tension reference guide," can be found under https://www.fastenal.com/content/merch_rules/images/fcom/content-library/Torque-Tension Reference Guide.pdf, **2022**.

Electrochemical Healing of Fractured Metals

Zakaria Hsain, Mostafa Akbari, Adhokshid Prasanna, Zhimin Jiang, Masoud Akbarzadeh, James H. Pikul

Empowered by a quantitative predictive framework, room-temperature area-selective nickel electrodeposition with a single commonly used electrolyte enables 100 % restoration of tensile strength in a variety of fractured metals, including “unweldable” alloys and a 3D-printed complex structure. This framework could potentially enable a universal approach to repair fractured metals of various compositions, geometries, and length scales.